ACCSCIENCE PUBLISHING

International Journal of Bioprinting

RESEARCH ARTICLE

pH-responsive polydopamine-coated mesoporous silica nanoplatform integrated into 3D-printed PLA/nHA scaffolds for synergistic bone regeneration

Yaoxiang Xu[1,2,3,4†], Yali Li[1†], Jinpeng Liu[1,2], Yao Yu[1,2], Ming Sun[1,2], Xiao Zhang[1,2], Zexian Xu[1,2,3,4*], and Jian Sun[1,2,3,4*]

[1]The Affiliated Hospital of Qingdao University, Qingdao, Shandong, China

[2]School of Stomatology, Qingdao University, Qingdao, Shandong, China

[3]Dental Digital Medicine and 3D Printing Engineering Laboratory of Qingdao, School of Stomatology, Qingdao University, Qingdao, Shandong, China

Abstract

Integrating stimuli-responsive nanoplatforms into 3D-printed scaffolds offers a sophisticated approach to mimicking the complex microenvironment of bone healing while minimizing the side effects associated with high-dose growth factor therapy. This study reports the design of a mesoporous silica-based dual-drug delivery system co-loaded with dexamethasone (DEX) and bone morphogenetic protein-2 (BMP-2) to harness their synergistic osteogenic potential while minimizing BMP-2-associated side effects. Mesoporous silica nanoparticles (MSNs) were synthesized to encapsulate DEX, followed by a polydopamine (PDA) coating formed via self-polymerization under mild alkaline conditions. BMP-2 was subsequently immobilized on the PDA layer, yielding pH-responsive DEX@MSNs/PDA/BMP-2 nanoparticles. Characterization confirmed uniform morphology, efficient loading, and controlled release, with accelerated release under acidic conditions, mimicking bone-defect environments. *In vitro*, dual-drug nanoparticles promoted osteogenic differentiation of preosteoblasts in a concentration-dependent manner, as evidenced by increased alkaline phosphatase activity, enhanced calcium deposition, and upregulated osteogenic genes. The nanoparticles were incorporated into three-dimensionally (3D)-printed polylactic acid/nano-hydroxyapatite scaffolds via freeze-drying, yielding composites with favorable porosity, mechanical properties, hydrophilicity, and biodegradability. In a rat calvarial defect model, implantation of the composite scaffolds significantly improved bone regeneration and neovascularization relative to controls, as demonstrated by micro-computed tomography and histological analyses. The results demonstrate that PDA-coated MSNs co-delivering DEX and BMP-2, integrated into 3D-printed scaffolds, provide a biocompatible and effective platform for bone tissue engineering. This approach combines pH-responsive release, dual-drug synergy, and structural support, offering translational potential for mandibular defect repair.

Keywords: Mesoporous silica; Polydopamine; Bone morphogenetic protein-2; Dexamethasone; Bone repair; Composite scaffold

†*These authors contributed equally to this work.*

***Corresponding authors:**
Zexian Xu
(xuzexian@qdu.edu.cn)
Jian Sun
(sunjianqdfy@qdu.edu.cn)

Citation: Xu Y, Li Y, Liu J, *et al*. pH-responsive polydopamine-coated mesoporous silica nanoplatform integrated into 3D-printed PLA/nHA scaffolds for synergistic bone regeneration. *Int J Bioprint*. 2026:12(2):026020016. doi: 10.36922/IJB026020016

Received: January 10, 2026

Revised: March 10, 2026

Accepted: March 17, 2026

Published online: April 30, 2026

Copyright: © 2026 Author(s). This is an Open-Access article distributed under the terms of the Creative Commons Attribution License, permitting distribution, and reproduction in any medium, provided the original work is properly cited.

Publisher's Note: AccScience Publishing remains neutral with regard to jurisdictional claims in published maps and institutional affiliations.

1. Introduction

Extensive mandibular defects resulting from tumors, infections, injuries, and congenital or acquired deformities frequently occur in oral and maxillofacial conditions. These issues notably influence a patient's facial aesthetics, oral capabilities, and mental health.[1,2] Currently, autologous bone grafting is considered the gold standard for mandibular defect repair. Alternative options, such as allografts, xenografts, and bone substitutes, face several limitations, including donor-site morbidity, limited bone availability, inadequate morphological matching, immune rejection, and the risk of disease transmission.[3,4] Bone tissue engineering, an interdisciplinary technique that integrates seed cells, growth factors, and tissue-engineered scaffolds into a three-dimensional osteogenic system, shows promising applications in bone repair.[5,6]

Bone morphogenetic protein-2 (BMP-2) is a frequently utilized growth factor known for its bone-forming efficacy and is essential in the development of bone tissue engineering strategies.[7,8] However, to achieve therapeutic efficacy, the clinical application of BMP-2 often requires doses significantly higher than its physiological levels in natural bone.[9] High doses of BMP-2 can lead to side effects such as inflammatory responses, ectopic bone formation, and tumor induction.[10,11] Studies have shown that basic fibroblast growth factor, vascular endothelial growth factor, and platelet-rich plasma enhance the osteogenic effects of BMP-2, exhibiting synergistic effects when combined.[12–15] Given that growth factors are complex to prepare, expensive, and prone to inactivation, the incorporation of small molecules such as dexamethasone (DEX) represents a strategic approach to enhance the osteogenic efficacy of BMP-2 through potent synergistic effects.[16–21]

To harness the synergistic osteogenic potential of BMP-2 and DEX, an effective dual-drug delivery system is essential. Mesoporous silica nanoparticles (MSNs) have emerged as premier drug carriers due to their tunable particle size, adjustable pore channels, and exceptional biocompatibility.[22,23] The abundance of silanol groups on MSN surfaces allows for versatile modifications with functional groups that act as "mesoporous gates" that enable controlled drug release in response to stimuli such as pH, enzymes, or light.[24,25] However, while the mesoporous structure of MSNs is well-suited for loading small molecules like DEX, it possesses inherent limitations in delivering macromolecules such as proteins.[26,27] The emergence of polydopamine (PDA), a mussel-inspired biomaterial, provides a new approach for immobilizing macromolecules like proteins on nanoparticles.[3,28] PDA surfaces possess a wealth of active functional groups, including phenolic hydroxyl, quinone, amino, and imino groups. These groups are reactive in Michael addition or Schiff-base reactions with nucleophilic groups, such as amino (–NH2) or thiol (–SH) groups. This makes PDA a versatile platform for immobilizing biomolecules, with broad applications in drug delivery, tissue engineering, and biosensing.[23,29,30] Furthermore, the pH-sensitivity of PDA allows it to function as a responsive gatekeeper, accelerating drug release under the acidic conditions typical of bone defect environments.[31,32] In this study, we utilized the mesopores of MSNs to encapsulate DEX and employed a PDA coating as both a pH-responsive gate and a functional platform for immobilizing BMP-2. This strategy yielded dual-drug-loaded nanoparticles (DEX@MSNs/PDA/BMP-2), and we subsequently investigated their release kinetics and synergistic osteogenic efficacy.

Tissue-engineered scaffolds, serving as osteogenic microenvironments, are indispensable in bone tissue engineering.[6,33] Polylactic acid (PLA), known for its excellent mechanical properties and biocompatibility, is widely utilized in tissue-engineered scaffolds. Over time, PLA degrades into carbon dioxide and water, which are naturally absorbed by the body.[33,34] Despite its advantages, PLA has several limitations, including local aseptic inflammation due to degradation, hydrophobicity that hinders cell adhesion, and the lack of osteoconductivity and osteoinductivity, which restrict its use.[35] Hydroxyapatite (HA) is a key constituent of bone, known for its excellent biocompatibility and ability to support bone growth. However, its lack of a three-dimensional (3D) porous structure makes it less favorable for cell adhesion and growth.[36] Composite scaffolds made of PLA and HA can effectively complement each other's shortcomings, making them ideal for tissue-engineered scaffolds.[35,37] Furthermore, 3D-printing technology, aided by computer assistance, can create customized, precise, and multilevel tissue-engineered scaffolds with excellent shapes and mechanical properties. These scaffolds provide a conducive environment for osteogenic cell recruitment, vascular growth, and nutrient metabolism.[38,39]

Beyond conventional applications of PDA solely for surface modification, the innovation of this work lies in the multifunctional integration of PDA as both a pH-responsive gatekeeper and a protein-anchoring platform. Specifically, the PDA coating simultaneously modulates DEX release from mesoporous silica channels and provides a versatile interface for the stable immobilization of BMP-2. By incorporating these dual-functional nanoparticles into 3D-printed PLA/nano-HA (nHA) scaffolds, we developed a hierarchical delivery system capable of responding to the localized microenvironment of bone defects. Following the *in vitro* evaluation of the nanoparticles' osteogenic

potential, the therapeutic efficacy of the composite scaffolds was validated in a rat calvarial defect model. This integrated strategy, which combines stimuli-responsive nanomedicine with 3D-printed architecture, offers a promising approach to repairing critical-sized bone defects.

2. Materials and methods

2.1. Materials

Polylactic acid (grade 4032D) was purchased from Natureworks (United States of America [USA]). nHA (<100 nm), dopamine hydrochloride, cetyltrimethylammonium bromide (CTAB), tetraethyl orthosilicate (TEOS), DEX, L-ascorbic acid sodium, and pentobarbital sodium were purchased from Sigma-Aldrich (USA). Recombinant human BMP-2 (rhBMP-2) and its corresponding enzyme-linked immunosorbent assay (ELISA) kit were procured from Abmole (USA) and Sigma-Aldrich (USA), respectively.

For biological assays, mouse embryonic osteoblast precursor cells (MC3T3-E1) were purchased from Cyagen Biosciences (China). Alpha-modified Eagle's medium (α-MEM), fetal bovine serum (FBS), and penicillin-streptomycin were purchased from Gibco (USA). Fluorescein isothiocyanate, phalloidin, and 4,6-diamidino-2-phenylindole were procured from Sigma-Aldrich (USA). The PrimeScript RT kit (RR036A, Takara, Japan), TRIzol reagent (Invitrogen, USA), and genetic primers (Thermo Fisher, USA) were used for molecular analysis. Sprague-Dawley rats (8 weeks old, n = 27) were acquired from Pengyue Laboratory Animal Breeding Co., Ltd. (China). Deionized water was used throughout the study.

2.2. Preparation of mesoporous silica nanoparticles

Mesoporous silica nanoparticles were prepared following the procedure described in a previous study.[40] Briefly, 1.0 g of CTAB and 0.28 g of sodium hydroxide were dissolved in 480 mL of deionized water. The mixture was continuously stirred and heated to 80 °C until it completely dissolved. Subsequently, 5 mL of TEOS was gradually added to the mixture and stirred continuously for 2 h. The final product was centrifuged at 8,000 rpm for 10 min, followed by multiple washes with both water and ethanol. The sample was dispersed in a mixture of 500 mL of ethanol and 5 mL of hydrochloric acid (HCl), then refluxed at 80 °C for 24 h. The sample underwent centrifugation and was thoroughly washed several times to eliminate the CTAB template. Ultimately, the template-free MSNs were collected using centrifugation, cleansed, and dried under vacuum to yield MSN powder. This powder was then sterilized with ultraviolet (UV) light, preparing it for further application.

2.3. Preparation of dexamethasone-loaded mesoporous silica nanoparticles and drug loading capacity measurement

An ethanolic solution of DEX at 4 mg/mL was prepared. Subsequently, 100 mg of MSNs was combined with 2 mL of the DEX solution and incubated in the dark for 24 h. After centrifugation, the pellet was rinsed three times with deionized water and then dried under vacuum in a freeze-dryer (Alpha 2-4LSC BASIC, Christ, Germany), yielding DEX-loaded MSNs (DEX@MSNs). The absorbance at 242 nm was measured for both the collected washing solution and the supernatant.[41] The drug loading capacity of DEX was calculated using **Equation 1**:

$$\text{Loading capacity}(\%) = \frac{\text{Mass of DEX added} - \text{Mass of DEX in solution}}{\text{Total mass of DEX} - \text{loaded nanoparticles}} \times 100\% \quad (1)$$

2.4. Preparation of polydopamine-coated dexamethasone-loaded mesoporous silica nanoparticles and drug loading capacity measurement

To synthesize nanoparticles with a PDA coating, 100 mg of DEX@MSNs were suspended in 50 mL of tris-HCl solution (10 mM, pH 8.5). Next, 50 mg of dopamine hydrochloride was added, and the solution was stirred at room temperature in the dark for 12 h to form a PDA layer.[3] The DEX@MSNs/PDA nanoparticles were collected via centrifugation, followed by three washes with deionized water to eliminate residual unpolymerized dopamine. Subsequently, the nanoparticles were freeze-dried. The collected wash solution and supernatant were evaluated by measuring the absorbance at 242 nm using a UV spectrophotometer (UV-3600i Plus, Shimadzu, Japan).

2.5. Preparation of polydopamine-coated dexamethasone- and bone morphogenetic protein-2-loaded mesoporous silica nanoparticles and drug loading capacity measurement

A 4 mL solution containing BMP-2 (4 μg/mL) was prepared. Then, 100 mg of DEX@MSNs/PDA nanoparticles were added to the solution, followed by continuous stirring at 4 °C for 4 h.[3,42] The mixture was centrifuged, and the pellet was freeze-dried for 24 h, yielding nanoparticles co-loaded with DEX and BMP-2 (DEX@MSNs/PDA/BMP-2). The supernatant was used to measure BMP-2 concentration using a BMP-2 ELISA kit. The BMP-2 loading capacity was

subsequently determined.

2.6. Characterization of nanoparticles

To examine the surface morphology and size of the nanoparticles, scanning electron microscopy (SEM; Sigma 300, ZEISS, Germany) and transmission electron microscopy (TEM; JEM-2100Plus, JEOL, Japan) were employed. The particle size and zeta potential were assessed using a dynamic light scattering instrument (Zetasizer Nano ZS90, Malvern, UK). Nitrogen adsorption–desorption isotherms were recorded to determine the specific surface area and pore size distribution using an automated surface area and porosity analyzer (Micromeritics ASAP 2460, USA). The measurement process was analyzed using the Brunauer–Emmett–Teller (BET) and Barret–Joyner–Halenda methods. Nanoparticle chemical functional groups were examined using Fourier-transform infrared spectroscopy (FTIR; Nicolet iS20, Thermo Scientific, USA). X-ray diffraction (XRD; SmartLab SE, Rigaku Corporation, Japan) was employed to analyze the mesoporous structure of the nanoparticles, investigating both the small-angle ($2\theta < 10°$) and wide-angle scattering regions.

2.7. *In vitro* release of dexamethasone

The DEX@MSNs and DEX@MSNs/PDA nanoparticles (20 mg each) were dispersed in 1 mL of phosphate-buffered saline (PBS) at different pH values (7.4, 6.0, and 5.0) and enclosed in dialysis membranes (molecular weight cutoff: 3,500 Da). The dialysis membranes were placed in centrifuge tubes containing 4 mL of PBS at the corresponding pH and incubated in a thermostatic orbital shaker (LD-DY1, Shandong Laiende Intelligent Technology Co., Ltd., China) at 37 °C and 100 rpm.[40] At predetermined time points (every 2 days for a total of 28 days starting from day 1, with 3 days of dialysis at the last time point), 2 mL of the release medium was removed and replaced with fresh PBS. The absorbance at 242 nm was recorded using a UV spectrophotometer. The amount of DEX released was calculated based on the loading capacity, and the release profiles were plotted.

2.8. *In vitro* release of bone morphogenetic protein-2

The DEX@MSNs/PDA/BMP-2 nanoparticles (50 mg) were introduced into multiple 10 mL centrifuge tubes containing 5 mL of PBS at varying pH values (7.4, 6.0, and 5.0). At predetermined time points (every 2 days for a total of 21 days, starting from day 1), the samples were centrifuged, and the supernatant was collected. BMP-2 concentrations were quantified using a BMP-2 ELISA kit according to the manufacturer's instructions. The amount of BMP-2 released was determined, and the release profiles were plotted.

2.9. Cytocompatibility test

The base medium consisted of high-glucose α-MEM supplemented with 10% FBS and 1% penicillin–streptomycin. Sterile centrifuge tubes were prepared, each containing 100 μg of MSNs, DEX@MSNs, DEX@MSNs/PDA, and DEX@MSNs/PDA/BMP-2. To prepare solutions at a concentration of 100 μg/mL, each type of nanoparticle was dispersed in 1 mL of base medium. Similarly, DEX@MSNs/PDA/BMP-2 solutions were prepared at concentrations of 50, 200, and 400 μg/mL for the experimental groups, whereas the control group received the base medium. Passage-4 MC3T3-E1 cells were maintained under standard culture conditions and then prepared as a suspension at a concentration of 2.5×10^4 cells/mL. A 100 μL cell suspension was seeded into 96-well plates (2.5×10^3 cells/well) and incubated at 37 °C under 5% CO_2 for 24 h. Subsequently, 100 μL of nanoparticle solution was added to each well in the experimental groups, whereas the control group received 100 μL of base medium. On days 1, 3, and 5, 10 μL of cell-counting kit (CCK)-8 solution was added to each well, followed by incubation for 2 h. Absorbance was measured at 450 nm using a microplate reader (Synergy H1MF, BioTek, USA). Cell viability was calculated using **Equation 2**:

$$\text{Cell viability}(\%) = \frac{A_{\text{Test}}}{A_{\text{Control}}} \times 100\% \quad (2)$$

where A_{Test} and A_{Control} indicate the absorbance measurements for the experimental and control groups, respectively, at a wavelength of 450 nm.

2.10. Alkaline phosphatase activity

MC3T3-E1 cells were seeded in 12-well plates at a concentration of 4×10^5 cells/cm^2. The negative control group received the base medium (Control), while the positive control group (Osteoinductive) was cultured in osteogenic induction medium (base medium supplemented with 10 mM β-glycerophosphate, 50 μg/mL ascorbic acid, and 0.1 μM DEX).[40] Nanoparticle suspensions for the experimental groups were prepared by dispersing MSNs, DEX@MSNs, DEX@MSNs/PDA, and DEX@MSNs/PDA/BMP-2 nanoparticles in the base medium at 100 μg/mL. In addition, DEX@MSNs/PDA/BMP-2 nanoparticle suspensions were prepared at concentrations of 50, 200, and 400 μg/mL. After osteogenic induction for 7 and 14 days, the cells were washed three times with PBS and then fixed with 4% paraformaldehyde for 30 min. After three additional PBS washes, 5-bromo-4-chloro-3-indolyl phosphate/nitro blue tetrazolium solution was added to completely cover the cells, and staining was performed

for 30 min. The stain was then removed, and the cells were rinsed three times with distilled water. Images were acquired using a microscope. A 1% Triton X-100 solution was used to lyse the cells. The lysate was transferred to Eppendorf tubes and centrifuged at 12,000 rpm for 30 min at 4 °C. The supernatant was carefully transferred to fresh Eppendorf tubes, and the optical density (OD) at 520 nm was measured using a microplate reader.

2.11. Alizarin Red staining

MC3T3-E1 cells were seeded in 24-well plates at a concentration of 4×10^5 cells/cm^2. After 14 and 21 days of culture, the cells were washed with PBS three times, fixed with 4% paraformaldehyde for 30 min, and subsequently washed three times with PBS. Cells underwent a 30-min treatment using a 2% Alizarin Red dye, followed by three washes with deionized water. Microscopic analysis was conducted to assess the presence of calcium deposits. To measure the staining of calcium-bound alizarin red, a solution of 100 nmol/L cetylpyridinium chloride (Sigma, USA) was applied to decolorize at room temperature for 1 h. Absorbance readings were obtained at 562 nm using a microplate reader (Synergy H1MF, BioTek, USA).

2.12. Osteogenic-related gene expression analysis

MC3T3-E1 cells were seeded in 12-well plates at a density of 4×10^5 cells/cm^2 and maintained at 37 °C for 14 days. The expression of osteogenic-related genes, including *Runx2*, *Col1a1*, and *Ocn*, was evaluated using real-time reverse transcription–polymerase chain reaction (RT–PCR). Using Trizol reagent, RNA was isolated, and cDNA was synthesized according to the instructions provided in the PrimeScript reverse transcription kit (RR036A, Takara, Japan). The synthesized cDNA was diluted tenfold using sterile distilled water, and 4 μL of the diluted cDNA was added to the SYBR Premix Ex TaqTM reaction mixture (Takara, Japan) for RT–PCR. The RT–PCR reaction mixture (10 μL) contained 4 μL diluted cDNA, 5 μL 1× SYBR Premix Ex Taq, 0.4 μL each of forward and reverse primers (0.2 μM), and 0.2 μL carboxy-X-rhodamine reference dye (50×). This was followed by 40 cycles of amplification, each including a 5-s denaturation at 95 °C and a 34-s annealing and extension at 60 °C. Table 1 shows the primer sequences used in RT–PCR analysis.

2.13. Preparation of DEX@MSNs/PDA/BMP-2-loaded polylactic acid/nano-hydroxyapatite composite scaffolds

The PLA powder (10 g) and nHA powder (2.5 g) were mixed at a ratio of 4:1 (w:w) in a 1,4-dioxane solution and stirred magnetically (500 rpm, 25 °C) for 30 min. The mixture was freeze-dried, and the resulting PLA/nHA material was loaded into a 3D printer (3D printing, Qingdao University of Technology, China) . Using computer-assisted design, cylindrical scaffolds with a diameter of 8 mm and a thickness of 1.5 mm were printed with specific parameters: line width 250 μm, layer thickness 200 μm, and pore size 300 μm. To load the scaffolds with nanoparticles, 100 mg of DEX@MSNs/PDA/BMP-2 nanoparticles were dispersed in 1 mL of deionized water. The PLA/nHA scaffolds were immersed in this suspension, followed by vacuum freeze-drying to obtain drug-loaded DEX@MSNs/PDA/BMP-2/PLA/nHA (D@M/P/B/PLA/nHA) composite scaffolds, which were stored at 4 °C for subsequent analysis.[43]

2.14. Characterization and performance testing of composite scaffolds

The surface morphology, porosity, and nanoparticle attachment of the composite scaffolds were observed using SEM. To assess hydrophilicity, the contact angle of each scaffold group was determined using a contact angle measurement device (SL 200B, Solon, China). A specific volume of anhydrous ethanol (V1) was poured into a beaker, and the scaffold was immersed in the liquid for 30 min until it was completely saturated, with no bubbles visible on the surface. The total volume (TV) of liquid was recorded as V2. The scaffold was subsequently removed, and the remaining volume of ethanol was recorded as V3. The porosity of the scaffold was calculated using **Equation 3**. The mechanical properties of the scaffolds (PLA/nHA and D@M/P/B/PLA/nHA) were tested using a universal testing machine (CMT6103, MTS, USA) with a load capacity of 5 kN and a constant compression speed of 1 mm/min. The mass of each scaffold was measured and

Table 1. Primer sequences for reverse transcription-polymerase chain reaction

Gene	Forward primer sequence (5'–3')	Reverse primer sequence (5'–3')
Runx2	TTCTCCAACCCACGAATGCAC	CAGGTACGTGTGGTAGTGAGT
Col1a1	AACATGACCAAAAACCAAAAGTG	CATTGTTTCCTGTGTCTTCTGG
Ocn	GAACAGACTCCGGCGCTA	AGGGAGGATCAAGTCCCG

recorded as M1. The scaffolds were subsequently immersed in 10 mL of PBS (pH 7.4) and incubated at 37 °C. At predetermined time points over a three-month period, the scaffolds were removed, washed, dried, and weighed again (M2). The degradation rate (%) was calculated using **Equation 4**. Degradation rate curves were plotted to analyze the temporal degradation behavior of the scaffolds.

$$P(\%) = \frac{V1 - V3}{V2 - V3} \times 100\% \quad (3)$$

$$\text{Degradation rate } (\%) = \frac{M1 - M2}{M1} \times 100\% \quad (4)$$

2.15. Cytocompatibility of composite scaffolds

Sterilized composite scaffolds were placed in 24-well plates and pre-soaked in base medium before cell seeding. The control group received base medium without scaffolds. MC3T3-E1 cells were seeded at a density of 2×10^4 cells/mL (100 µL per well) and incubated at 37 °C in a 5% CO_2 atmosphere. On days 1, 3, and 5, 10 µL of CCK-8 solution was added to each well, and the OD was measured at 450 nm. Cell morphology and growth were examined using a fluorescence microscope. The cell viability was calculated using **Equation 2**.

2.16. *In vivo* osteogenesis

Male Sprague-Dawley rats (aged 8 weeks, weighing 150–200 g, $n = 27$) were acquired from Pengyue Laboratory Animal Breeding Co., Ltd. (Jinan, China; license: SCXK [Lu] 2022 0006). All animal-related procedures were approved by the Qingdao University Experimental Animal Welfare Ethics Committee (No. 20230725SD2120240725057) and conducted in accordance with the regulations established by the Institutional Animal Care and Use Committee. A total of 27 rats were randomly allocated into three groups ($n = 9$ per group) using a computer-generated random sequence. Animals were housed in pairs under standard conditions (22 ± 2 °C, 12 h light/dark cycle) with *ad libitum* access to food and water. Postoperative health and behavior were monitored daily, and rats received intramuscular injections of penicillin sodium (200,000 U/day) for three consecutive days to prevent infection. Only rats that underwent the surgical procedure without intraoperative complications were included in the final analysis; no animals were excluded during the study.

The rats were anesthetized by an intraperitoneal administration of sodium pentobarbital (60 mg/kg). A trephine was used to create an 8 mm full-thickness cranial defect. Blank PLA/nHA scaffolds or D@M/P/B/PLA/nHA composite scaffolds were implanted into the defect sites. At 4, 8, and 12 weeks post-surgery, the cranial defects were examined using a micro-computed tomography (CT) system (Quantum GX2, PerkinElmer, Japan). The scanning was performed at a source voltage of 70 kV, maintaining a consistent spatial resolution of 12 µm for all samples to ensure high-fidelity imaging. Subsequently, the reconstructed data were analyzed using Analyze software (14.0, AnalyzeDirect, USA) to quantify key osteogenic parameters, including bone volume (BV), TV, bone mineral density (BMD), and BV fraction (BV/TV). Rats were euthanized at 4, 8, and 12 weeks for histological evaluation of cranial bones using hematoxylin and eosin (HE) and Masson staining.

2.17. Histopathological evaluation of major organs

The rats were euthanized at 4, 8, and 12 weeks after surgery. Their major organs, including the heart, liver, spleen, lungs, and kidneys, were harvested. These organs were then fixed in 4% paraformaldehyde, embedded in paraffin, and subsequently sectioned for HE staining. Healthy rats without surgical intervention served as controls. Histopathological changes were assessed to evaluate scaffold material toxicity.

2.18. Statistical analysis

All quantitative data are presented as mean ± standard deviation (SD). For *in vitro* experiments, at least three independent replicates ($n = 3$) were performed for each group. The study used Statistical Package for Social Sciences (SPSS 23.0, IBM, United States) for analysis. A one-way analysis of variance was utilized for group comparisons, with statistical significance set at $p < 0.05$.

3. Results

3.1. Nanoparticle characterization

Figure 1A displays the morphology of the four nanoparticle types, which were examined using SEM. The nanoparticles exhibited a spherical shape, consistent size, and displayed excellent dispersion with minimal clustering. The surfaces of MSNs and DEX@MSNs were smooth, whereas those of DEX@MSNs/PDA and DEX@MSNs/PDA/BMP-2 were rougher due to the PDA coating and BMP-2 loading. TEM micrographs (Figure 1B) showed that the nanoparticles were predominantly spherical, with sizes of 270–330 nm. The surfaces of MSNs and DEX@MSNs appeared smooth, with mesoporous structures clearly visible near the edges. The PDA coating on DEX@MSNs/PDA nanoparticles obscured the mesoporous structure, and granular loading material was visible on the surfaces of DEX@MSNs/PDA/BMP-2. As shown in Table 2, the Zeta potentials of MSNs, DEX@MSNs, DEX@MSNs/PDA, and DEX@MSNs/PDA/BMP-2 were −9.2 ± 0.7 mV, −8.4 ± 0.6 mV, −29.5 ± 1.1 mV, and −30.7 ± 0.9 mV, respectively, with particle sizes of

270.1 ± 13.1 nm, 280.9 ± 7.2 nm, 290.1 ± 8.7 nm, and 319.3 ± 6.9 nm (Figure 1C), respectively. The polydispersity indices were 0.340 ± 0.013, 0.214 ± 0.010, 0.127 ± 0.009, and 0.374 ± 0.015, respectively. The corresponding specific surface areas of the four nanoparticles were 620.7 ± 29.2 m^2/g, 496.3 ± 21.6 m^2/g, 93.2 ± 13.4 m^2/g, and 83.8 ± 9.7 m^2/g, respectively. The pore sizes of MSNs and DEX@MSNs were 3.1± 0.6 nm and 2.7 ± 0.4 nm, respectively, while no pore sizes could be detected for DEX@MSNs/PDA and DEX@MSNs/PDA/BMP-2. The nitrogen adsorption–desorption isotherms (Figure 1D) showed a typical type IV isotherm for MSNs, while DEX@MSNs, DEX@MSNs/PDA, and DEX@MSNs/PDA/BMP-2 deviated from the standard type IV isotherm. XRD analysis (Figure 1E) revealed characteristic peaks in the small-angle region (1.2–1.4°). The most prominent peak was observed in the MSN group, with varying degrees of attenuation in the other groups, which is consistent with previous reports.[41] FTIR spectra (Figure 1F) indicated characteristic peaks of Si–O–Si bending vibrations, Si–O–Si symmetric stretching vibrations, and Si–O asymmetric vibrations at 465 cm^{-1}, 800 cm^{-1}, and 1,080 cm^{-1}, respectively, characteristic of silica. Peaks at 1,665 cm^{-1} and 896 cm^{-1} corresponded to DEX, confirming its successful loading. Peaks at 3,400 cm^{-1}, 2,955 cm^{-1}, and 1,625 cm^{-1} indicated the presence of PDA, corresponding to $-NH_2$ groups, aromatic double-bond skeletal vibrations, and amine groups, respectively.[44]

3.2. Cytocompatibility test

The survival rate of MC3T3-E1 cells exposed to 100 μg/mL of MSNs, DEX@MSNs, DEX@MSNs/PDA, and various concentrations of DEX@MSNs/PDA/BMP-2 was

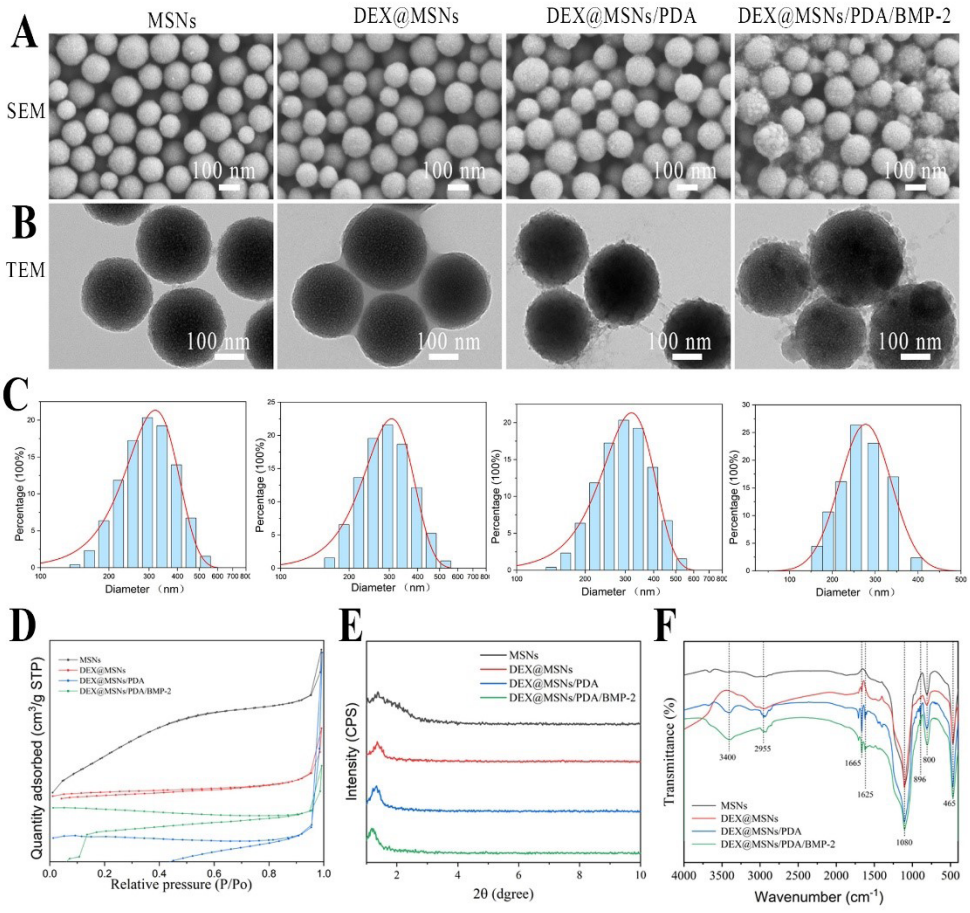

Figure 1. Characterization of nanoparticles. (A) SEM images of nanoparticles. Scale bar: 100 nm; magnification: 50000×. (B) TEM images of nanoparticles. Scale bar: 100 nm; magnification: 200000×. (C) Particle size distribution of nanoparticles. (D) Nitrogen adsorption-desorption isotherms of nanoparticles. (E) XRD analysis of nanoparticles. (F) FTIR spectra of nanoparticles.

Abbreviations: BMP-2: Bone morphogenic protein 2; CPS: Counts per second; DEX: Dexamethasone; FTIR: Fourier-transform infrared spectroscopy; MSNs: Mesoporous silica nanoparticles; PDA: Polydopamine; SEM: Scanning electron microscope; STP: Standard temperature and pressure; TEM: Transmission electron microscope; XRD: X-ray diffraction.

Table 2. Characterization of nanoparticles

Sample	Zeta potential (mV)	Size (nm)	PDI	BET surface area (m^2/g)	Pore size (nm)
A	−9.2 ± 0.7	270.1 ± 13.1	0.340 ± 0.013	620.7 ± 29.2	3.1
B	−8.4 ± 0.6	280.9 ± 7.2	0.214 ± 0.010	496.3 ± 21.6	2.7
C	−29.5 ± 1.1	290.1 ± 8.7	0.127 ± 0.009	93.2 ± 13.4	N/A
D	−30.7 ± 0.9	319.3 ± 6.9	0.374 ± 0.015	83.8 ± 9.7	N/A

Notes: (A) MSNs; (B) DEX@MSNs; (C) DEX@MSNs/PDA; (D) DEX@MSNs/PDA/BMP-2. Abbreviations: BET: Brunauer–Emmett–Teller; N/A: Not applicable; PDI: Polydispersity index.

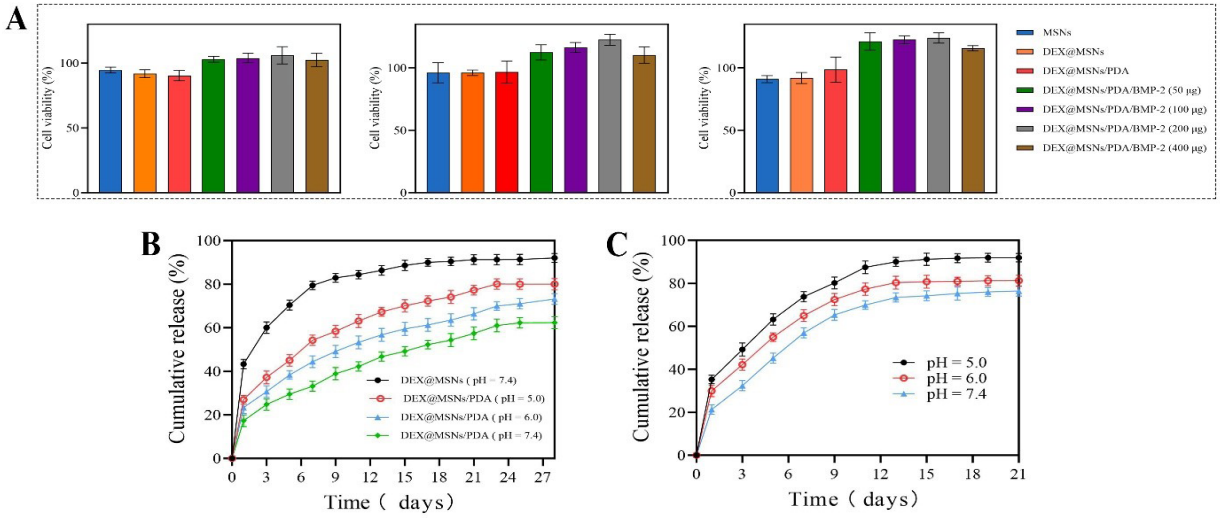

Figure 2. Cytocompatibility and drug release. (A) Cytocompatibility of nanoparticles. (B) DEX release profile. (C) BMP-2 release profile. Abbreviations: BMP-2: Bone morphogenic protein 2; DEX: Dexamethasone; MSNs: Mesoporous silica nanoparticles; PDA: Polydopamine.

evaluated on days 1, 3, and 5 (Figure 2A). Throughout the five-day period, each group demonstrated cell viability exceeding 90% relative to the control group, suggesting no significant cytotoxic effects. Throughout the study, DEX@MSNs/PDA/BMP-2 exhibited slightly higher cell viability compared to the other groups, maintaining high viability even at 400 μg/mL.

3.3. Dexamethasone loading and *in vitro* release

The DEX loading capacities of DEX@MSNs and DEX@MSNs/PDA were 25.82 ± 1.91 μg/mg and 24.73 ± 2.33 μg/mg, respectively, based on absorbance at 242 nm. Figure 2B illustrates the release patterns of DEX observed in vitro. At pH 7.4, DEX@MSNs exhibited rapid release, with 43.22% released on day 1, and cumulative releases of 79.45% and 92.01% on days 7 and 28, respectively. DEX@MSNs/PDA demonstrated a prolonged release profile, maintaining sustained release, and exhibited an increased release rate as the pH decreased. At pH 5.0, 6.0, and 7.4, the drug release from DEX@MSNs/PDA on day 1 were 27.01%, 23.34%, and 17.27%, respectively; on day 7, cumulative release achieved 54.27%, 44.34%, and 33.18%, and by day 28, 80.01%, 73.16%, and 62.30%, respectively.

3.4. Bone morphogenic protein-2 loading and *in vitro* release

The BMP-2 loading capacity of DEX@MSNs/PDA/BMP-2 was 43.27 ± 3.18 ng/mg, determined using the rhBMP-2 ELISA kit. Figure 2C presents the release profiles of BMP-2. Release was observed across all pH conditions, with faster release at acidic pH. At pH 5.0, 6.0, and 7.4, the release rates on day 1 were 35.28%, 29.97%, and 21.27%, respectively; on day 7, cumulative releases achieved 73.77%, 64.96%, and 56.94%; and by day 21, 91.92%, 81.29%, and 76.37%, respectively.

3.5. Alkaline phosphatase activity

The alkaline phosphatase (ALP) staining was conducted on days 7 and 14 in the MC3T3-E1 cell cultures (Figure 3A). At all time points, the DEX@MSNs/PDA/BMP-2 group exhibited the strongest ALP staining, followed by the Osteoinductive group, while other groups showed lighter staining. Quantitative assessment (Figure 3B–E) showed that by day 7, the ALP activity in the DEX@MSNs/PDA/BMP-2 group was notably elevated compared to the control, MSNs, DEX@MSNs, and DEX@MSNs/PDA groups. The ALP activity observed in the DEX@MSNs/PDA group was marginally elevated compared to the MSNs and DEX@MSNs groups, though the difference did not achieve statistical significance. ALP levels increased with nanoparticle concentration up to 100 μg/mL, with no additional increase observed at 200 μg/mL. After 14 days, all groups showed increased ALP activity compared to day 7, but the increases in MSNs, DEX@MSNs, and DEX@MSNs/PDA groups were minimal and not statistically significant. The ALP activity of the DEX@MSNs/PDA/BMP-2 group was significantly higher than that of other groups and showed concentration-dependent activity up to 100 μg/mL, with no further increase at 200 μg/mL.

3.6. Alizarin Red staining

Following a 14-day culture period, Alizarin Red staining was examined under a microscope (Figure 4A). Among all groups, the DEX@MSNs/PDA/BMP-2 group showed the most intense staining, the osteoinductive group being slightly less pronounced, whereas the remaining groups exhibited moderate staining. By day 21, staining in the DEX@MSNs/PDA/BMP-2 and Osteoinductive groups significantly deepened, with slight increases in other groups. Quantitative assessment of Alizarin Red staining (Figure 4B–E) revealed that on day 14, with a nanoparticle concentration of 100 μg/mL, the DEX@MSNs/PDA/BMP-2 group demonstrated the most calcium deposition, markedly surpassing other nanoparticle groups and the Control group ($p < 0.001$). Within the concentration range of 0–100 μg/mL, the DEX@MSNs/PDA/BMP-2

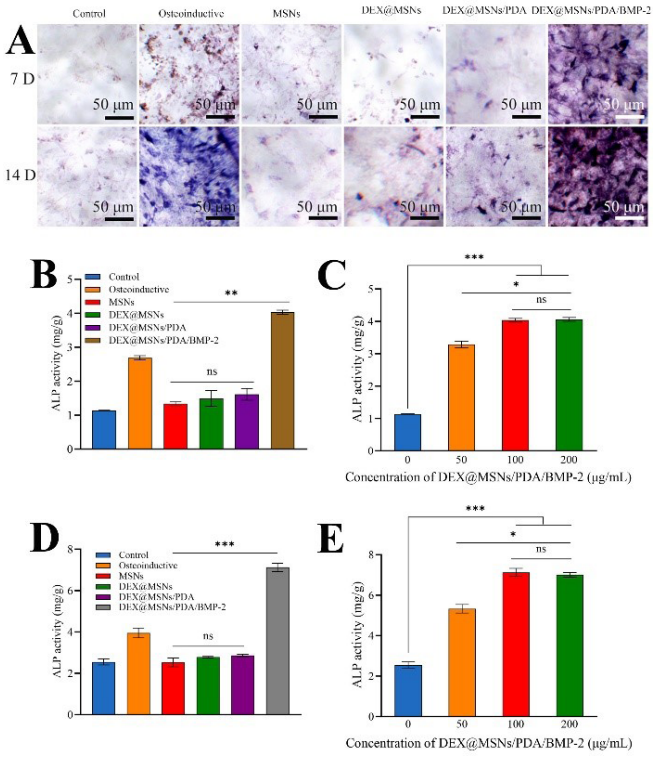

Figure 3. ALP activity in MC3T3-E1 cells treated with nanoparticles. (A) ALP staining of MC3T3-E1 cells on days 7 and 14. Scale bar: 50 μm; magnification:. 100×. (B) ALP activity of MC3T3-E1 cells treated with nanoparticles at 100 μg/mL on day 7. (C) ALP activity of MC3T3-E1 cells treated with DEX@MSNs/PDA/BMP-2 nanoparticles (0–200 μg/mL) on day 7. (D) ALP activity of MC3T3-E1 cells treated with nanoparticles at 100 μg/mL on day 14. (E) ALP activity of MC3T3-E1 cells treated with DEX@MSNs/PDA/BMP-2 nanoparticles (0–200 μg/mL) on day 14. Notes: $n = 3$ per group; $^{*}p < 0.05$; $^{**}p < 0.01$; $^{***}p < 0.001$.

Abbreviations: ALP: Alkaline phosphatase; BMP-2: Bone morphogenic protein 2; DEX: Dexamethasone; MSNs: Mesoporous silica nanoparticles; ns: No significant difference; PDA: Polydopamine.

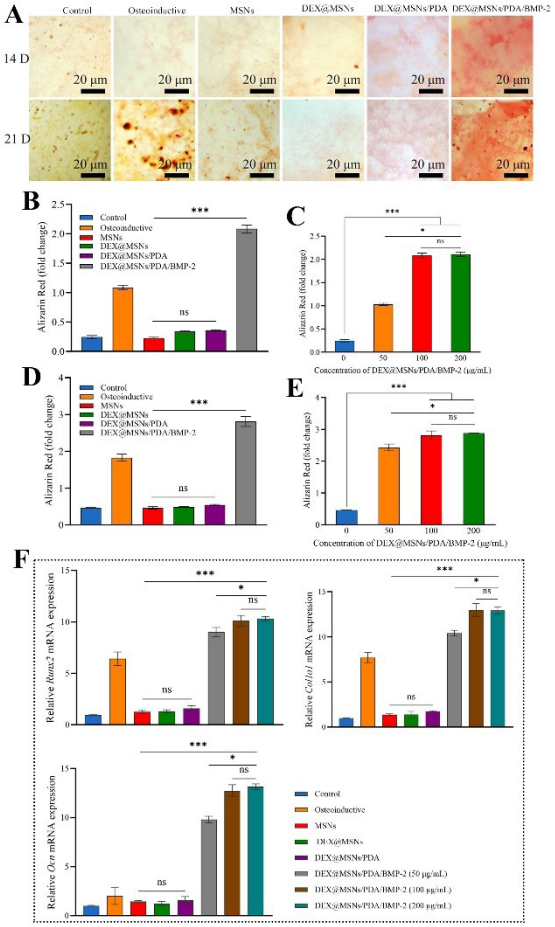

Figure 4. Alizarin Red staining and osteogenic-related gene expression in MC3T3-E1 cells treated with nanoparticles. (A) Alizarin Red staining on days 14 and 21. Scale bar: 20 μm; magnification: 100×. (B) Quantitative analysis of Alizarin Red staining on cells treated with nanoparticles (100 μg/mL) on day 14. (C) Quantitative analysis of Alizarin Red staining on cells treated with DEX@MSNs/PDA/BMP-2 nanoparticles (0–200 μg/mL) on day 14. (D) Quantitative analysis of Alizarin Red staining on cells treated with nanoparticles at a concentration of 100 μg/mL on day 21. (E) Quantitative analysis of Alizarin Red staining on cells treated with DEX@MSNs/PDA/BMP-2 nanoparticles (0–200 μg/mL) on day 21. (F) The expression of osteogenic-related genes in cells treated with nanoparticles (*Runx2*, *Col1a1*, and *Ocn*).
Notes: $n = 3$ per group; $^{*}p < 0.05$; $^{**}p < 0.01$; $^{***}p < 0.001$.
Abbreviations: BMP-2: Bone morphogenic protein 2; DEX: Dexamethasone; MSNs: Mesoporous silica nanoparticles; ns: No significant difference; PDA: Polydopamine.

group showed an increase in calcium deposition that corresponded to the concentration, but no further increase was observed at 200 μg/mL. On day 21, calcium deposition increased in all groups, with the 100 and 200 μg/mL concentrations of DEX@MSNs/PDA/BMP-2 showing the most pronounced effects, and no significant difference between these two concentrations.

3.7. Osteogenic-related gene expression

After 14 days of culture, the expression of osteogenic-related genes *Runx2*, *Col1a1*, and *Ocn* was assessed (Figure 4F). The DEX@MSNs/PDA/BMP-2 group exhibited the most elevated gene expression, coming after the Osteoinductive group, which was significantly higher than the Control, MSNs, DEX@MSNs, and DEX@MSNs/PDA groups ($p < 0.001$). Gene expression in the DEX@MSNs/PDA/BMP-2 group increased with concentration in the range of 0–100 μg/mL, but did not increase further at 200 μg/mL. Gene expression in the Control, MSNs, DEX@MSNs, and DEX@MSNs/PDA groups was low, with no significant differences among the groups ($p > 0.05$).

3.8. Characterization of composite scaffolds

As shown in Figure 5A, the 3D-printed PLA/nHA scaffolds matched the designed dimensions, appearing cylindrical with regular pores and smooth surfaces. After

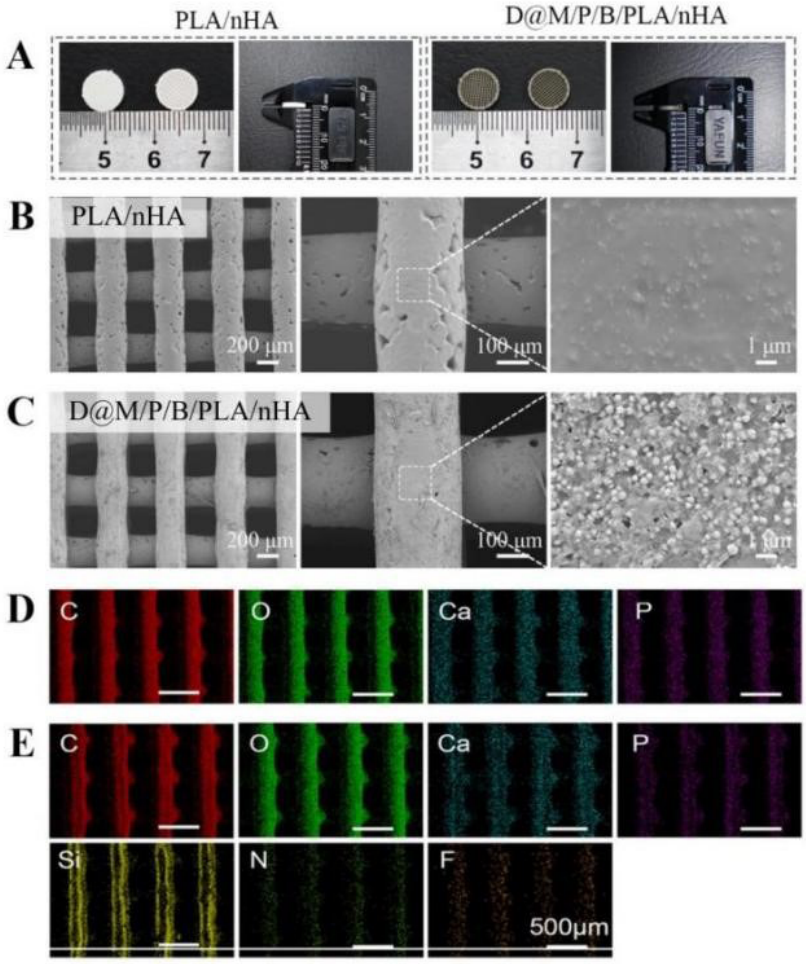

Figure 5. Characterization of composite scaffolds. (A) Macroscopic images of composite scaffolds. (B) SEM images of the PLA/nHA scaffolds. Scale bars: 200 μm, 100 μm, 1 μm; magnifications: 50×, 150×, 10000×. (C) SEM images of the D@M/P/B/PLA/nHA scaffolds. Scale bars: 200 μm, 100 μm, 1 μm; magnifications: 50×, 150×, 10000×. (D) Mapping analysis of the PLA/nHA scaffolds. Scale bar: 500 μm; magnification: 50×. (E) Mapping analysis of the D@M/P/B/PLA/nHA scaffolds. Scale bar: 500 μm; magnification: 50×.

Abbreviations: C: Carbon; Ca: Calcium; D@M/P/B: Dexamethasone@mesoporous silica nanoparticle/polydopamine/bone morphogenic protein 2; F: Fluorine; N: Nitrogen; nHA: Nano-hydroxyapatite; O: Oxygen; P: Phosphorus; PLA: Polylactic acid; SEM: Scanning electron microscope; Si: Silicon.

loading with dual-drug nanoparticles, the composite scaffold's morphology showed no significant changes, but turned from white to brownish, and the surface became rougher. SEM images of the scaffold microstructure (Figure 5B,C) revealed consistent, interconnected porous structures. At a lower magnification (scale bar = 50× μm), the scaffolds exhibited pore sizes of approximately 300 μm, with no significant structural deformation observed after nanoparticle loading. Observation at a higher magnification (scale bar = 150× μm) showed that the composite scaffold possessed a strut width (line width) of approximately 250 μm; notably, the surface of the blank scaffolds appeared smooth, whereas the nanoparticle-loaded scaffolds exhibited a distinctly rough morphology. High-resolution imaging (scale bar = 10000× μm) further revealed granular nHA components embedded within the PLA matrix of the PLA/nHA scaffolds, while the DEX@MSNs/PDA/BMP-2 nanoparticles were clearly visible and uniformly distributed on the surface of the composite scaffolds. Mapping analysis (Figure 5D,E) indicated that PLA/nHA scaffolds primarily contained carbon, oxygen, calcium, and phosphorus, while the composite scaffold (D@M/P/B/PLA/nHA) included additional elements, silicon, nitrogen, and fluorine.

3.9. Hydrophilicity of composite scaffolds

As shown in Figure 6A, the initial contact angles of PLA/nHA and D@M/P/B/PLA/nHA scaffolds were 97.6 ± 2.5° and 85.3 ± 2.7°, respectively, with the latter being significantly lower. Dynamic contact angle testing (Figure

6A) showed that water droplets on D@M/P/B/PLA/nHA scaffolds infiltrated almost completely within 5 s and fully infiltrated within 20 s, while PLA/nHA scaffolds required 120 and 160 s, respectively, indicating the superior hydrophilicity of the composite scaffold.

3.10. Porosity and mechanical properties of composite scaffolds

The porosity of PLA/nHA and D@M/P/B/PLA/nHA scaffolds was 77.6 ± 3.2% and 76.5 ± 2.9%, respectively (Figure 6B), indicating that nanoparticle loading did not significantly alter porosity. The compressive strengths of PLA/nHA and D@M/P/B/PLA/nHA scaffolds were 7.79 ± 0.06 MPa and 7.49 ± 0.08 MPa, respectively (Figure 6D).

3.11. Degradation of composite scaffolds

The degradation rates of PLA/nHA and D@M/P/B/PLA/nHA scaffolds are shown in Figure 6F. Both scaffolds degraded gradually over 12 weeks, with degradation rates of 47.9 ± 3.1% and 52.7 ± 2.3%, respectively; the composite scaffold degraded faster. SEM images (Figure 6E) revealed morphological changes during degradation. After four weeks, PLA/nHA scaffolds remained intact with a roughened surface, while D@M/P/B/PLA/nHA scaffolds exhibited localized cracking, exposing internal fiber structures. After eight weeks, blank scaffolds showed partial fractures and structural disruption, whereas drug-loaded scaffolds exhibited more extensive degradation with disrupted connections. By 12 weeks, blank scaffolds showed significant degradation with disrupted surface and internal structures, and drug-loaded scaffolds showed extensive degradation of both surface and internal structures.

3.12. Cytocompatibility of composite scaffolds

The results for the CCK-8 assay (Figure 6G) showed that cell viability in both scaffold groups exceeded that of the control group on days 1, 3, and 5, indicating promotion of cell proliferation. At all time points, D@M/P/B/PLA/nHA scaffolds exhibited higher cell activity than PLA/nHA scaffolds. Fluorescence microscopy (Figure 6E) showed an increase in cell numbers over time in all groups, with clear cell outlines, elongated or polygonal shapes, and well-spread morphology. Cell nuclei were stained blue, and cytoskeletons were clearly visible, with no signs of rupture or other abnormalities.

3.13. *In vivo* osteogenesis in rats

The repair effects of cranial defects in each group were evaluated using Micro-CT at weeks 4, 8, and 12 post-surgery. As shown in the 3D reconstruction results (Figure 7B), in the Control group, most of the cranial defect area remained empty at week 4, with only minimal new bone formation at the edges. In the PLA/nHA and D@M/P/B/PLA/nHA scaffold groups, no significant bone resorption was observed at the defect edges, and new bone grew along the scaffold surfaces, with the D@M/P/B/PLA/nHA group exhibiting more new bone formation than the PLA/nHA group. At weeks 8 and 12, the Control group showed no substantial increase in new bone, with large areas of bone defect remaining visible. Both scaffold groups exhibited continued new bone formation on their surfaces, with the D@M/P/B/PLA/nHA group showing more pronounced effects than the PLA/nHA group. As the scaffolds degraded, their internal pore structures became visible.

Quantitative examination of BV/TV (Figure 7C) revealed that at week 4, the D@M/P/B/PLA/nHA group exhibited significantly higher values than the Control group ($p < 0.001$) and the PLA/nHA group ($p < 0.01$). At week 8, BV/TV increased in all groups, with the drug-loaded scaffold group showing significantly higher values than the Control and PLA/nHA groups ($p < 0.001$). At week 12, the D@M/P/B/PLA/nHA group remained significantly higher than the other two groups. BMD results (Figure 7D) showed that at week 4, BMD values for the Control, PLA/nHA, and D@M/P/B/PLA/nHA groups were 1.24 ± 0.16 g/cm^3, 1.27 ± 0.09 g/cm^3, and 1.33 ± 0.13 g/cm^3, respectively. At weeks 8 and 12, BMD slightly increased, with the drug-loaded group showing higher values than the other two groups ($p < 0.05$).

The results of HE staining (Figure 7A) demonstrated the osteogenic effects in each group. At week 4, no inflammatory or pathological bone resorption was observed in any group. In the Control group, bone formation was limited to the periphery of the defect, with fibrous connective tissue predominantly filling the interior. In the PLA/nHA scaffold group, new bone formed at the base of the defect area, with bone matrix and lacunae containing osteocytes visible. The scaffold gaps were filled with fibrous connective tissue and a small amount of collagen fibers. In the D@M/P/B/PLA/nHA group, more new bone was observed at the scaffold base compared to the PLA/nHA group, with bone matrix formation and new blood vessels in the scaffold gaps. At week 8, no significant increase in new bone formation was observed in the Control group, and the defect area was primarily filled with fibrous connective tissue. The PLA/nHA scaffold group exhibited slight increases in new bone at the scaffold surface and base. In the D@M/P/B/PLA/nHA group, new bone extended into the scaffold pores, with significant bone coverage on the scaffold base and surface. At week 12, the cranial defect in the Control group remained largely unchanged compared to week 8. In the PLA/nHA scaffold group, additional new bone

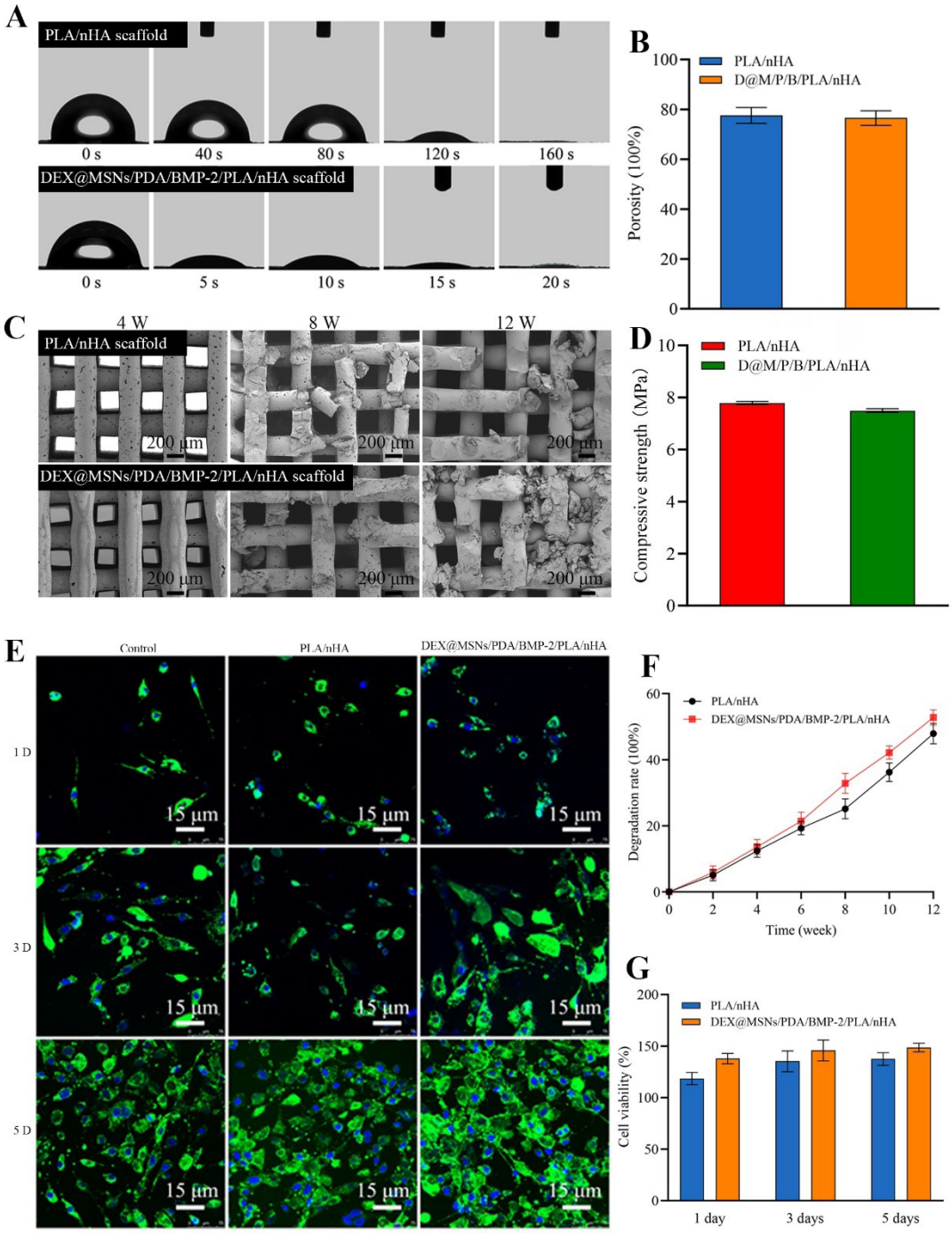

Figure 6. Physicochemical properties of composite scaffolds. (A) Hydrophilicity of composite scaffolds. (B) Porosity of composite scaffolds. (C) SEM images of composite scaffolds degradation. Scale bar: 200 μm; magnification: 50×. (D) Mechanical properties of composite scaffolds. (E) Fluorescence microscopy of composite scaffolds seeded with MC3T3-E1 cells. Scale bar: 15 μm; magnification: 200×. (F) Degradation of composite scaffolds. (G) Cytocompatibility of composite scaffolds.

Abbreviations: BMP-2: Bone morphogenic protein 2; DEX: Dexamethasone; MSNs: Mesoporous silica nanoparticles; nHA: Nano-hydroxyapatite; ns: No significant difference; PDA: Polydopamine; PLA: Polylactic acid; SEM: Scanning electron microscope.

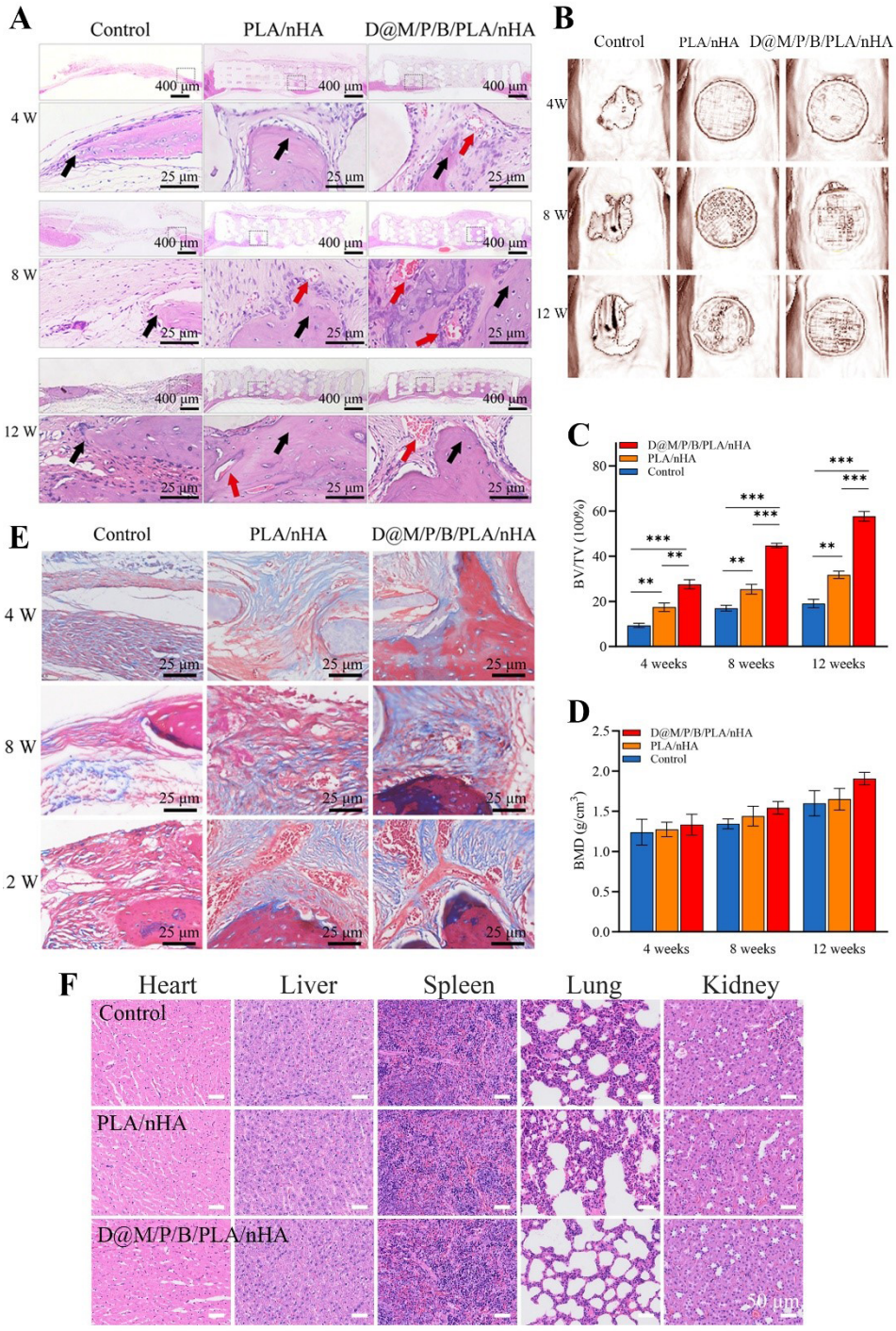

Figure 7. *In vivo* osteogenesis. (A) Micro-computed tomography images at weeks 4, 8, and 12 post-surgery. (B) Quantitative analysis of bone volume fraction. (C) Bone mineral density. (D) Hematoxylin and eosin staining of cranial defects. Scale bar: 400 μm, 25 μm; magnification: 40×, 200×. (E) Masson staining of cranial defects. Scale bar: 25 μm; magnification: 200×. (F) Histopathological analysis of major organs. Scale bar: 50 μm; magnification: 40×.
Notes: $n = 3$ per group; $^{**}p < 0.01$; $^{***}p < 0.001$.
Abbreviations: BMD: Bone mineral density; BV: Bone volume; D@M/P/B: Dexamethasone@mesoporous silica nanoparticle/polydopamine/bone morphogenic protein 2; nHA: Nano-hydroxyapatite; PLA: Polylactic acid; TV: Total volume.

was observed at the base, with scaffold pores primarily filled with fibrous connective tissue and a small amount of collagen fibers, and localized areas containing small blood vessels. In the group with drug-loaded scaffolds, the base of the scaffold was occupied by newly formed bone, while the pores were predominantly filled with bone and collagen fibers. Additionally, there was a significant presence of blood vessels. The results of Masson staining (Figure 7E) show that by week 4, the defect region in the control group was predominantly fibrous connective tissue. In the PLA/nHA scaffold group, fibrous connective tissue, along with a few collagen fibers, was observed, whereas the D@M/P/B/PLA/nHA scaffold group mainly consisted of collagen fibers. At weeks 8 and 12, fibrous connective tissue occupied the cranial defect in the Control group. In the PLA/nHA scaffold group, fibrous connective tissue remained predominant with a slight increase in collagen fibers, while the drug-loaded scaffold group showed a predominance of collagen fibers.

3.14. Histopathological analysis of major organs

Twelve weeks after surgery (Figure 7F), histological evaluations of major organs, including the heart, liver, spleen, lungs, and kidneys, showed no morphological or structural abnormalities in either the PLA/nHA or D@M/P/B/PLA/nHA scaffold groups compared to the Control group. No signs of bleeding, necrosis, inflammation, or cellular abnormalities were observed, confirming that the scaffold materials caused no significant toxicity to the major organs of the rats.

4. Discussion

The physicochemical properties of MSNs, such as morphology, particle size, surface charge, and hydrophilicity, influence their adhesion and penetration ability, cellular uptake, and endosomal escape in physiological processes. Smaller nanoparticles (<20 nm) are rapidly cleared due to low cellular uptake, while larger particles are blocked by mucosal barriers and expelled. Nanoparticles around 300 nm in size are primarily internalized by cells through endocytosis.[31] Gu *et al.*[45] synthesized MSNs with carboxyl modifications in sizes of 250 nm, 350 nm, and 450 nm as cisplatin carriers. *In vitro* studies showed that 350 nm MSNs exhibited the highest enrichment efficiency in HeLa cells, effectively inhibiting cell activity. The shape of nanoparticles—such as spherical, rod-like, or dendritic—also significantly affects cellular uptake and cytotoxicity.[27] Dias *et al.*[46] fabricated spherical and rod-like gold-core silica-based nanoparticles (Au-MSSs) to examine the effects of particle shape on cellular uptake, reactive oxygen species (ROS) generation, penetration, and effects on cancer cells. Their results demonstrated that spherical Au-MSSs reduced ROS levels in cancer cells, showed more uniform distribution, and exhibited stronger penetration into 3D tumor spheroids, whereas rod-like Au-MSSs displayed improved cell migration and uptake, as well as higher cytotoxicity in cell cultures. Our study yielded spherical MSNs with an average particle diameter of 270 nm. After loading DEX, the particle size increased to 280.9 nm. Upon PDA coating and BMP-2 loading, the particle size further increased to 290.1 nm and 319.3 nm, respectively, indicating a gradual increase in size with drug incorporation and PDA coating.

Cell membranes, primarily composed of lipid bilayers and membrane proteins, typically carry a negative surface charge. Positively charged nanoparticles tend to aggregate and nonspecifically bind to serum proteins and normal tissues, leading to rapid clearance by the reticuloendothelial system from the bloodstream.[47] Thus, surface charge is a critical attribute for nanoparticles. All four types of nanoparticles prepared in this study carried a negative charge, facilitating their cellular uptake. Specific surface area is closely related to drug-loading capacity. The specific surface area of MSNs was 620.7 m^2/g, which decreased to 496.3 m^2/g after loading DEX, likely due to DEX entering the mesopores. The specific surface areas of DEX@MSNs/PDA and DEX@MSNs/PDA/BMP-2 further decreased, indicating that the PDA coating blocked the mesopores. XRD is commonly used to characterize mesoporous materials. MSNs showed a diffraction peak in the small-angle region at 1.3°, confirming their mesoporous structure. The diffraction peaks of other nanoparticles were reduced to varying degrees, particularly after incorporating DEX and applying the PDA coating, indicating a reduction or elimination of mesopores. In the present study, the stability of DEX@MSNs/PDA/BMP-2 nanoparticles in protein-rich environments is supported by the inherent physicochemical properties of the PDA coating. It is well established that PDA, characterized by its abundant hydrophilic catechol and amine groups, forms a robust hydration layer that minimizes non-specific serum protein adsorption.[48] This "anti-fouling" property, coupled with the strong negative surface charge (zeta potential) observed in our study, provides sufficient electrostatic and steric repulsion to prevent nanoparticle aggregation in physiological media.[49] Such stability is indirectly confirmed by our drug-release data and the high cell viability in serum-supplemented medium, where significant aggregation or protein fouling would otherwise have compromised the pH-responsive release kinetics and cellular uptake.

As drug carriers, MSNs must preserve the activity of BMP-2 and DEX, avoiding phenomena such as "premature release" or "burst release" before reaching the target site

to ensure sustained and controlled drug release. Studies have shown that MSNs enter cells primarily via energy-dependent endocytosis, forming endosomes, which subsequently fuse with lysosomes.[31,50] Our study simulated the drug release profiles of BMP-2 and DEX under conditions mimicking physiological environments (pH = 7.4), endosomes (pH = 6.0–6.5), and lysosomes (pH = 5.0–5.5). DEX@MSNs, lacking effective mesopore sealing, exhibited rapid drug release, with 43.22% of DEX released on the first day and a cumulative release of 79.45% within a week. Such rapid release may lead to excessive local DEX concentrations, which are unfavorable for osteogenesis. After PDA coating, DEX@MSNs/PDA demonstrated sustained release at pH 5.0, 6.0, and 7.4, with faster release at lower pH values. This indicates that PDA effectively seals mesopores and exhibits pH-responsive behavior. Analysis of BMP-2 release curves showed sustained release across all tested pH values, with faster release at lower pH, suggesting that as PDA degrades, the BMP-2 release rate accelerates accordingly.

In vitro osteogenesis analysis, including ALP activity, calcium deposition, and PCR detection of osteogenesis-related genes, yielded consistent results. At the same concentration of 100 μg/mL, DEX@MSNs/PDA/BMP-2 exhibited the strongest osteogenic expression, indicating significant promotion of osteogenesis at this concentration. Within the range of 0–100 μg/mL, DEX@MSNs/PDA/BMP-2 promoted osteogenic differentiation in a concentration-dependent manner. However, osteogenesis did not further increase at 200 μg/mL, suggesting that the synergistic effect of BMP-2 and DEX occurs within a specific concentration range. This may be due to higher particle concentrations, leading to excessive local DEX concentrations, which can inhibit cell proliferation and osteogenic differentiation. It is noteworthy that the osteogenic promotion effect of DEX@MSNs/PDA/BMP-2 reached a plateau at a nanoparticle concentration of 200 μg/mL. This concentration-dependent behavior likely stems from the biphasic effect of DEX on bone metabolism. While physiological or low doses of DEX are known to promote osteoblastic differentiation by upregulating *Runx2* and BMP-2 receptors, excessive concentrations of glucocorticoids have been shown to exert inhibitory effects. High-dose DEX can suppress osteoblast proliferation, reduce the synthesis of Type I collagen, and even trigger apoptosis via the activation of glucocorticoid receptors and subsequent oxidative stress pathways.[51,52] Therefore, the optimized loading and release kinetics in our system are designed to maintain the local DEX concentration within a beneficial range, avoiding the detrimental effects associated with high-dose glucocorticoid exposure. Beyond its direct osteogenic synergy with BMP-2, the inclusion of DEX plays a pivotal role in osteo-immunomodulation.

Bone healing initiates with a complex inflammatory cascade; if prolonged, this inflammation can lead to fibrous encapsulation rather than ossification. As highlighted by recent studies, the early release of anti-inflammatory agents can mitigate the secretion of pro-inflammatory factors like tumor necrosis factor-α and interleukin-6, thereby fostering a pro-regenerative microenvironment.[53] In our system, the initial release of DEX likely facilitates the resolution of early-stage inflammation, priming the defect site for the potent osteoinductive signals provided by BMP-2. Other studies have shown that silicon ions promote the proliferation of bone marrow mesenchymal stem cells, the formation of mineralized nodules, and the expression of osteogenesis-related genes.[54] In our study, MSNs, DEX@MSNs, and DEX@MSNs/PDA exhibited slightly higher osteogenic activity than the Control group, which may be attributed to the release of silicon ions during MSN degradation. However, as inorganic particles with high physicochemical stability, MSNs degrade slowly, resulting in a minimal contribution to osteogenesis promotion.

Recent advances in 3D-printing technology enable the fabrication of customized scaffolds tailored to the geometry of bone defects, advancing bone tissue engineering.[35,38] In the current study, PLA was selected as the scaffold material for its excellent biocompatibility and degradability, complemented by the osteoconductivity, acid-neutralizing properties, and mechanical strength enhancement provided by nHA. Using 3D printing, PLA/nHA scaffolds were fabricated and then combined with dual-drug-loaded MSNs via freeze-drying to construct D@M/P/B/PLA/nHA composite scaffolds. This method is straightforward, preserves drug activity, and provides an effective strategy for integrating nanoparticles into tissue-engineering scaffolds. The scaffold architecture exerts a "secondary regulation" effect on the drug-release kinetics. While the free DEX@MSNs/PDA/BMP-2 nanoparticles exhibit precise pH-responsive gatekeeping, their integration into the 3D-printed PLA/nHA matrix introduces additional steric hindrance and tortuous diffusion pathways. This secondary barrier effect likely contributes to a more attenuated release profile, which is beneficial for maintaining effective local drug concentrations throughout the multistage process of bone defect repair.

Research on tissue engineering scaffolds has evolved from focusing solely on macroscopic structures to optimizing microscopic structures. Studies have shown that pore sizes smaller than 75 μm are suitable for fibrous tissue growth, sizes between 75–100 μm are optimal for immature bone tissue, and sizes larger than 200 μm are ideal for fully mineralized bone tissue. Bone tissue formation requires

pore sizes of at least 100–150 μm, while vascularization demands a minimum pore size of 300 μm.[55] The scaffolds fabricated in this study had pore sizes of approximately 300 μm, providing adequate space for bone and vascular formation and facilitating vascular ingrowth. In addition to internal porosity, surface roughness and hydrophilicity of scaffold materials are critical parameters for cell adhesion and proliferation. Hydrophilicity tests revealed that the drug-loaded composite scaffolds exhibited smaller contact angles, with water droplets infiltrating the scaffolds within five seconds, indicating good hydrophilicity, likely attributable to the inclusion of drug-loaded nanoparticles. The increase in hydrophilicity can be reliably attributed to the chemical modifications of the PDA coating and BMP-2. Furthermore, measuring the apparent contact angle directly on the scaffold provides a more biologically relevant representation of the microenvironment encountered by cells during initial adhesion compared to a flat film, confirming that improved wettability facilitates cell infiltration and protein adsorption within the 3D porous structure.

Bone primarily consists of trabecular (cancellous) bone and cortical bone. Trabecular bone, located internally, has low density, contains blood vessels, is porous (porosity: 30–90%), and has a compressive strength ranging from 7–10 MPa, serving as the primary site for nutrient metabolism. Cortical bone, located externally, is highly mineralized, with a porosity of 5–30% and compressive strength of 130–225 MPa.[56] Typically, higher porosity improves cell adhesion and osteogenic efficiency but reduces mechanical strength, making it crucial to balance porosity and mechanical strength.[57] In this study, the porosity of PLA/nHA and D@M/P/B/PLA/nHA scaffolds was 77.6 ± 3.2% and 76.5 ± 2.9%, respectively, with compressive strengths of 7.79 ± 0.06 MPa and 7.49 ± 0.08 MPa, respectively, fully meeting the requirements for trabecular bone in terms of porosity and mechanical properties. Scaffold degradability is another critical consideration, as the degradation rate should match the rate of osteogenesis, ensuring minimal scaffold remnants in the newly formed bone area. To date, no scaffold material has achieved an optimal balance between degradation rate, osteogenesis rate, porosity, and mechanical properties. In our study, the degradation rates of PLA/nHA and D@M/P/B/PLA/nHA scaffolds at 12 weeks were 47.9 ± 3.1% and 52.76 ± 2.31%, respectively. The faster degradation rate of the drug-loaded scaffold compared to the blank scaffold may be attributed to its better hydrophilicity.

The Micro-CT analysis reveals that 12 weeks after surgery, the Control group exhibited minimal bone formation along the margins of the bone defect. This demonstrates that the 8-mm cranial defect qualifies as a "critical-sized bone defect," which cannot heal spontaneously. In the PLA/nHA and D@M/P/B/PLA/nHA groups, new bone grew along the scaffold surfaces, with the drug-loaded composite scaffold group exhibiting more new bone formation than the blank scaffold group, indicating that the drug-loaded composite scaffold effectively promoted bone regeneration. The BV/TV results further corroborated this finding. HE and Masson staining results revealed that the drug-loaded scaffold group exhibited the best osteogenic performance. Most of the scaffold pores in this group were filled with bone matrix, while the remaining space was primarily occupied by unmineralized collagen fibers. In contrast, the blank scaffold group showed less bone formation, with scaffold gaps filled with fibrous connective tissue and a small amount of collagen fibers. The Control group primarily displayed fibrous connective tissue in the defect area. These findings confirm the superior osteogenic effects and sustained bone formation capability of the drug-loaded scaffold group. Notably, the drug-loaded scaffold group exhibited significant vascular ingrowth, indicating that the scaffold not only promoted bone formation but also enhanced angiogenesis. This can be attributed to the scaffold's optimal pore size and porosity, which provide an environment conducive to vascular infiltration and growth.

5. Conclusion

This study emphasizes the dual-functional role of PDA as a pH-sensitive gatekeeper for DEX and a stable immobilization platform for BMP-2, moving beyond its traditional use as a simple surface coating. By integrating these dual-drug-loaded nanoparticles into 3D-printed PLA/nHA scaffolds, a hierarchical, microenvironment-responsive delivery system was fabricated. Following *in vitro* characterization of the nanoparticles' osteogenic performance, the composite scaffolds demonstrated superior bone-repairing efficacy in a rat calvarial defect model. This synergistic approach, coupling stimuli-responsive nanocarriers with 3D-printed structural supports, provides a sophisticated strategy for bone tissue engineering and the treatment of large-scale osseous defects.

Acknowledgments

None.

Funding

This research was funded by the Qingdao Stomatology Climbing Peak Project (grant number: 2022-11-29-07), Development and Clinical Application of a Mental Disease Diagnostic System Based on Facial Expressions and

Multidimensional Physiological Signals (grant number: 25-1-5-smjk-19-nsh) and the Clinical Medicine+X Project of Qingdao University Hospital (grant number: QDFY+X2023207).

Conflict of interest

The authors declare they have no competing interests.

Author contributions

Conceptualization: Jian Sun
Data curation: Jinpeng Liu
Formal analysis: Xiao Zhang
Funding acquisition: Jian Sun
Investigation: Ming Sun
Methodology: Yao Yu
Project administration: Zexian Xu
Resources: Yaoxiang Xu
Supervision: Zexian Xu
Validation: Yali Li
Visualization: Jinpeng Liu
Writing–original draft: Yaoxiang Xu
Writing–review and editing: Yali Li

Ethics approval and consent to participate

The study was approved by the Qingdao University Experimental Animal Welfare Ethics Committee (No. 20230725SD2120240725057) and conducted in accordance with the regulations established by the Institutional Animal Care and Use Committee.

Consent for publication

Not applicable.

Availability of data

The data that support the findings of this study are available from the corresponding author upon reasonable request.

References

1. Zhang Q, Wu W, Qian C, *et al*. Advanced biomaterials for repairing and reconstruction of mandibular defects. *Mater Sci Eng C Mater Biol Appl*. 2019;103:109858.

   doi: 10.1016/j.msec.2019.109858

2. Dalfino S, Savadori P, Piazzoni M, *et al*. Regeneration of Critical-Sized Mandibular Defects Using 3D-Printed Composite Scaffolds: A Quantitative Evaluation of New Bone Formation in In Vivo Studies. *Adv Healthc Mater*. 2023;12(21):e2300128.

   doi: 10.1002/adhm.202300128

3. Sun H, Dong J, Wang Y, *et al*. Polydopamine-Coated Poly(l-lactide) Nanofibers with Controlled Release of VEGF and BMP-2 as a Regenerative Periosteum. *ACS Biomater Sci Eng*. 2021;7(10):4883-4897.

   doi: 10.1021/acsbiomaterials.1c00246

4. Yang Z, Xie L, Zhang B, *et al*. Preparation of BMP-2/PDA-BCP Bioceramic Scaffold by DLP 3D Printing and its Ability for Inducing Continuous Bone Formation. *Front Bioeng Biotechnol*. 2022;10:854693.

   doi: 10.3389/fbioe.2022.854693

5. Adel IM, ElMeligy MF, Amer MS, Elkasabgy NA. Polymeric nanocomposite hydrogel scaffold for jawbone regeneration: The role of rosuvastatin calcium-loaded silica nanoparticles. *Int J Pharm X*. 2023;6:100213.

   doi: 10.1016/j.ijpx.2023.100213

6. Bertsch C, Marechal H, Gribova V, *et al*. Biomimetic Bilayered Scaffolds for Tissue Engineering: From Current Design Strategies to Medical Applications. *Adv Healthc Mater*. 2023;12(17):e2203115.

   doi: 10.1002/adhm.202203115

7. Gillman CE, Jayasuriya AC. FDA-approved bone grafts and bone graft substitute devices in bone regeneration. *Mater Sci Eng C Mater Biol Appl*. 2021;130:112466.

   doi: 10.1016/j.msec.2021.112466

8. Howard MT, Wang S, Berger AG, *et al*. Sustained release of BMP-2 using self-assembled layer-by-layer film-coated implants enhances bone regeneration over burst release. *Biomaterials*. 2022;288:121721.

   doi: 10.1016/j.biomaterials.2022.121721

9. Ma D, An G, Liang M, Liu Y, Zhang B, Wang Y. A composited PEG-silk hydrogel combining with polymeric particles delivering rhBMP-2 for bone regeneration. *Mater Sci Eng C Mater Biol Appl*. 2016;65:221-231.

   doi: 10.1016/j.msec.2016.04.043

10. Gelebart P, Cuenot S, Sinquin C, *et al*. Microgels based on Infernan, a glycosaminoglycan-mimetic bacterial exopolysaccharide, as BMP-2 delivery systems. *Carbohydr Polym*. 2022;284:119191.

    doi: 10.1016/j.carbpol.2022.119191

11. Oliver-Cervello L, Martin-Gomez H, Mandakhbayar N, *et al*. Mimicking Bone Extracellular Matrix: From BMP-2-Derived Sequences to Osteogenic-Multifunctional Coatings. *Adv Healthc Mater*. 2022;11(20):e2201339.

    doi: 10.1002/adhm.202201339

12. Stamnitz S, Krawczenko A, Szalaj U, *et al*. Osteogenic Potential of Sheep Mesenchymal Stem Cells Preconditioned with BMP-2 and FGF-2 and Seeded on an nHAP-Coated PCL/HAP/beta-TCP Scaffold. *Cells*. 2022;11(21).

    doi: 10.3390/cells11213446

13. Nedorubova IA, Bukharova TB, Mokrousova VO, *et al*.

Comparative Efficiency of Gene-Activated Matrices Based on Chitosan Hydrogel and PRP Impregnated with BMP2 Polyplexes for Bone Regeneration. *Int J Mol Sci*. 2022;23(23).

doi: 10.3390/ijms232314720

14. Liu K, Meng CX, Lv ZY, *et al*. Enhancement of BMP-2 and VEGF carried by mineralized collagen for mandibular bone regeneration. *Regen Biomater*. 2020;7(4):435-440.

doi: 10.1093/rb/rbaa022

15. Geng Y, Duan H, Xu L, *et al*. BMP-2 and VEGF-A modRNAs in collagen scaffold synergistically drive bone repair through osteogenic and angiogenic pathways. *Commun Biol*. 2021;4(1):82.

doi: 10.1038/s42003-020-01606-9

16. Huang Y, Lin Y, Rong M, Liu W, He J, Zhou L. 20(S)-hydroxycholesterol and simvastatin synergistically enhance osteogenic differentiation of marrow stromal cells and bone regeneration by initiation of Raf/MEK/ERK signaling. *J Mater Sci Mater Med*. 2019;30(8):87.

doi: 10.1007/s10856-019-6284-0

17. Bakshi R, Hokugo A, Zhou S, *et al*. Application of Hydroxycholesterols for Alveolar Cleft Osteoplasty in a Rodent Model. *Plast Reconstr Surg*. 2019;143(5):1385-1395.

doi: 10.1097/PRS.0000000000005528

18. Park JB. Combination of simvastatin and bone morphogenetic protein-2 enhances the differentiation of osteoblasts by regulating the expression of phospho-Smad1/5/8. *Exp Ther Med*. 2012;4(2):303-306.

doi: 10.3892/etm.2012.590

19. Wei A, Leong A, Williams L, *et al*. BMP-7 in combination with estrogen enhances bone formation in a fracture callus explant culture. *Tohoku J Exp Med*. 2010;221(1):61-68.

doi: 10.1620/tjem.221.61

20. Chen PY, Sun JS, Tsuang YH, Chen MH, Weng PW, Lin FH. Simvastatin promotes osteoblast viability and differentiation via Ras/Smad/Erk/BMP-2 signaling pathway. *Nutr Res*. 2010;30(3):191-199.

doi: 10.1016/j.nutres.2010.03.004

21. Pauly S, Luttosch F, Morawski M, Haas NP, Schmidmaier G, Wildemann B. Simvastatin locally applied from a biodegradable coating of osteosynthetic implants improves fracture healing comparable to BMP-2 application. *Bone*. 2009;45(3):505-511.

doi: 10.1016/j.bone.2009.05.010

22. Zou Y, Huang B, Cao L, Deng Y, Su J. Tailored Mesoporous Inorganic Biomaterials: Assembly, Functionalization, and Drug Delivery Engineering. *Adv Mater*. 2021;33(2):e2005215.

doi: 10.1002/adma.202005215

23. Xu B, Li S, Shi R, Liu H. Multifunctional mesoporous silica nanoparticles for biomedical applications. *Signal Transduct Target Ther*. 2023;8(1):435.

doi: 10.1038/s41392-023-01654-7

24. Vivero-Escoto JL, Slowing, II, Trewyn BG, Lin VS. Mesoporous silica nanoparticles for intracellular controlled drug delivery. *Small*. 2010;6(18):1952-1967.

doi: 10.1002/smll.200901789

25. Tang F, Li L, Chen D. Mesoporous silica nanoparticles: synthesis, biocompatibility and drug delivery. *Adv Mater*. 2012;24(12):1504-1534.

doi: 10.1002/adma.201104763

26. Wen J, Yang K, Liu F, Li H, Xu Y, Sun S. Diverse gatekeepers for mesoporous silica nanoparticle based drug delivery systems. *Chem Soc Rev*. 2017;46(19):6024-6045.

doi: 10.1039/c7cs00219j

27. Wang Y, Gou K, Guo X, Ke J, Li S, Li H. Advances in regulating physicochemical properties of mesoporous silica nanocarriers to overcome biological barriers. *Acta Biomater*. 2021;123:72-92.

doi: 10.1016/j.actbio.2021.01.005

28. Wang Z, Jia Z, Jiang Y, *et al*. Mussel-inspired nano-building block assemblies for mimicking extracellular matrix microenvironments with multiple functions. *Biofabrication*. 2017;9(3):035005.

doi: 10.1088/1758-5090/aa7fdc

29. Salve R, Kumar P, Ngamcherdtrakul W, Gajbhiye V, Yantasee W. Stimuli-responsive mesoporous silica nanoparticles: A custom-tailored next generation approach in cargo delivery. *Mater Sci Eng C Mater Biol Appl*. 2021;124:112084.

doi: 10.1016/j.msec.2021.112084

30. Lerida-Viso A, Estepa-Fernandez A, Garcia-Fernandez A, Marti-Centelles V, Martinez-Manez R. Biosafety of mesoporous silica nanoparticles; towards clinical translation. *Adv Drug Deliv Rev*. 2023;201:115049.

doi: 10.1016/j.addr.2023.115049

31. Ding L, Zhu X, Wang Y, *et al*. Intracellular Fate of Nanoparticles with Polydopamine Surface Engineering and a Novel Strategy for Exocytosis-Inhibiting, Lysosome Impairment-Based Cancer Therapy. *Nano Lett*. 2017;17(11):6790-6801.

doi: 10.1021/acs.nanolett.7b03021

32. Chang D, Gao Y, Wang L, *et al*. Polydopamine-based surface modification of mesoporous silica nanoparticles as pH-sensitive drug delivery vehicles for cancer therapy. *J Colloid Interface Sci*. 2016;463:279-287.

doi: 10.1016/j.jcis.2015.11.001

33. Baptista R, Guedes M. Morphological and mechanical characterization of 3D printed PLA scaffolds with controlled

porosity for trabecular bone tissue replacement. *Mater Sci Eng C Mater Biol Appl*. 2021;118:111528.

doi: 10.1016/j.msec.2020.111528

34. Li Z, Tang S, Shi Z, *et al*. Multi-scale cellular PLA-based bionic scaffold to promote bone regrowth and repair. *Int J Biol Macromol*. 2023;245:125511.

doi: 10.1016/j.ijbiomac.2023.125511

35. Hwangbo H, Lee J, Kim G. Mechanically and biologically enhanced 3D-printed HA/PLLA/dECM biocomposites for bone tissue engineering. *Int J Biol Macromol*. 2022;218:9-21.

doi: 10.1016/j.ijbiomac.2022.07.040

36. Zhou K, Yu P, Shi X, *et al*. Hierarchically Porous Hydroxyapatite Hybrid Scaffold Incorporated with Reduced Graphene Oxide for Rapid Bone Ingrowth and Repair. *ACS Nano*. 2019;13(8):9595-9606.

doi: 10.1021/acsnano.9b04723

37. Hassanajili S, Karami-Pour A, Oryan A, Talaei-Khozani T. Preparation and characterization of PLA/PCL/HA composite scaffolds using indirect 3D printing for bone tissue engineering. *Mater Sci Eng C Mater Biol Appl*. 2019;104:109960.

doi: 10.1016/j.msec.2019.109960

38. Wang W, Junior JRP, Nalesso PRL, *et al*. Engineered 3D printed poly(varepsilon-caprolactone)/graphene scaffolds for bone tissue engineering. *Mater Sci Eng C Mater Biol Appl*. 2019;100:759-770.

doi: 10.1016/j.msec.2019.03.047

39. Daly AC, Freeman FE, Gonzalez-Fernandez T, Critchley SE, Nulty J, Kelly DJ. 3D Bioprinting for Cartilage and Osteochondral Tissue Engineering. *Adv Healthc Mater*. 2017;6(22).

doi: 10.1002/adhm.201700298

40. Zhou X, Feng W, Qiu K, *et al*. BMP-2 Derived Peptide and Dexamethasone Incorporated Mesoporous Silica Nanoparticles for Enhanced Osteogenic Differentiation of Bone Mesenchymal Stem Cells. *ACS Appl Mater Interfaces*. 2015;7(29):15777-15789.

doi: 10.1021/acsami.5b02636

41. Zhou X, Zhang Q, Chen L, *et al*. Versatile Nanocarrier Based on Functionalized Mesoporous Silica Nanoparticles to Codeliver Osteogenic Gene and Drug for Enhanced Osteodifferentiation. *ACS Biomater Sci Eng*. 2019;5(2):710-723.

doi: 10.1021/acsbiomaterials.8b01110

42. Zhao X, Han Y, Li J, *et al*. BMP-2 immobilized PLGA/hydroxyapatite fibrous scaffold via polydopamine stimulates osteoblast growth. *Mater Sci Eng C Mater Biol Appl*. 2017;78:658-666.

doi: 10.1016/j.msec.2017.03.186

43. Singhawannurat S, Lawtae P, Rojviriya C, Phoovasawat C. Development of PLA/HA porous scaffolds with controlled pore sizes using the combined freeze drying and sucrose leaching technique for bone tissue engineering. *J Met Mater Miner*. 2024;34(2).

doi: 10.55713/jmmm.v34i2.1928

44. Razavi M, Primavera R, Kevadiya BD, *et al*. Controlled Nutrient Delivery to Pancreatic Islets Using Polydopamine-Coated Mesoporous Silica Nanoparticles. *Nano Lett*. 2020;20(10):7220-7229.

doi: 10.1021/acs.nanolett.0c02576

45. Gu J, Liu J, Li Y, Zhao W, Shi J. One-pot synthesis of mesoporous silica nanocarriers with tunable particle sizes and pendent carboxylic groups for cisplatin delivery. *Langmuir*. 2013;29(1):403-410.

doi: 10.1021/la3036264

46. Dias DR, Moreira AF, Correia IJ. The effect of the shape of gold core-mesoporous silica shell nanoparticles on the cellular behavior and tumor spheroid penetration. *J Mater Chem B*. 2016;4(47):7630-7640.

doi: 10.1039/c6tb02668k

47. Wang LS, Wu LC, Lu SY, *et al*. Biofunctionalized phospholipid-capped mesoporous silica nanoshuttles for targeted drug delivery: improved water suspensibility and decreased nonspecific protein binding. *ACS Nano*. 2010;4(8):4371-4379.

doi: 10.1021/nn901376h

48. Lynge ME, van der Westen R, Postma A, Stadler B. Polydopamine--a nature-inspired polymer coating for biomedical science. *Nanoscale*. 2011;3(12):4916-4928.

doi: 10.1039/c1nr10969c

49. Liu Y, Ai K, Lu L. Polydopamine and its derivative materials: synthesis and promising applications in energy, environmental, and biomedical fields. *Chem Rev*. 2014;114(9):5057-5115.

doi: 10.1021/cr400407a

50. Feng W, Nie W, He C, *et al*. Effect of pH-responsive alginate/chitosan multilayers coating on delivery efficiency, cellular uptake and biodistribution of mesoporous silica nanoparticles based nanocarriers. *ACS Appl Mater Interfaces*. 2014;6(11):8447-8460.

doi: 10.1021/am501337s

51. Zhao R, Tao L, Qiu S, *et al*. Melatonin rescues glucocorticoid-induced inhibition of osteoblast differentiation in MC3T3-E1 cells via the PI3K/AKT and BMP/Smad signalling pathways. *Life Sci*. 2020;257:118044.

doi: 10.1016/j.lfs.2020.118044

52. Huang W, Jin S, Yang W, *et al*. Protective effect of Agrimonia pilosa polysaccharides on dexamethasone-treated MC3T3-E1 cells via Wnt/beta-Catenin pathway. *J Cell Mol Med*. 2020;24(3):2169-2177.

doi: 10.1111/jcmm.14868

53. Bi Z, Cai Y, Shi X, *et al*. Macrophage-mediated immunomodulation in biomaterial-assisted bone repair: Molecular insights and therapeutic prospects. *Chem Eng J*. 2024;488.

doi: 10.1016/j.cej.2024.150631

54. Han P, Wu C, Xiao Y. The effect of silicate ions on proliferation, osteogenic differentiation and cell signalling pathways (WNT and SHH) of bone marrow stromal cells. *Biomater Sci*. 2013;1(4):379-392.

doi: 10.1039/c2bm00108j

55. Lin KF, He S, Song Y, *et al*. Low-Temperature Additive Manufacturing of Biomimic Three-Dimensional Hydroxyapatite/Collagen Scaffolds for Bone Regeneration. *ACS Appl Mater Interfaces*. 2016;8(11):6905-6916.

doi: 10.1021/acsami.6b00815

56. Wubneh A, Tsekoura EK, Ayranci C, Uludag H. Current state of fabrication technologies and materials for bone tissue engineering. *Acta Biomater*. 2018;80:1-30.

doi: 10.1016/j.actbio.2018.09.031

57. Kirillova A, Yeazel TR, Asheghali D, *et al*. Fabrication of Biomedical Scaffolds Using Biodegradable Polymers. *Chem Rev*. 2021;121(18):11238-11304.

doi: 10.1021/acs.chemrev.0c01200